Chinese Journal of Aeronautics, (2016), **xxx**(xx): xxx–xxx

CSAA

Chinese Society of Aeronautics and Astronautics
& Beihang University

Chinese Journal of Aeronautics

cja@buaa.edu.cn
www.sciencedirect.com

REVIEW ARTICLE

Modelling and simulation of flight control electromechanical actuators with special focus on model architecting, multidisciplinary effects and power flows

Fu Jian [a,b,*], **Jean-Charles Maré** [b], **Fu Yongling** [a]

[a] *School of Mechanical Engineering and Automation, Beihang University, Beijing 100083, China*
[b] *Institut Clément Ader (CNRS UMR 5312), INSA-Toulouse, Toulouse 31077, France*

Received 12 January 2016; revised 22 March 2016; accepted 22 April 2016

KEYWORDS

Bond Graph;
Electro-hydrostatic actuator;
Electromechanical actuator;
More electric aircraft;
Modelling;
Power-by-wire;
Power loss;
Simulation

Abstract In the aerospace field, electromechanical actuators are increasingly being implemented in place of conventional hydraulic actuators. For safety-critical embedded actuation applications like flight controls, the use of electromechanical actuators introduces specific issues related to thermal balance, reflected inertia, parasitic motion due to compliance and response to failure. Unfortunately, the physical effects governing the actuator behaviour are multidisciplinary, coupled and nonlinear. Although numerous multi-domain and system-level simulation packages are now available on the market, these effects are rarely addressed as a whole because of a lack of scientific approaches for model architecting, multi-purpose incremental modelling and judicious model implementation. In this publication, virtual prototyping of electromechanical actuators is addressed using the Bond-Graph formalism. New approaches are proposed to enable incremental modelling, thermal balance analysis, response to free-run or jamming faults, impact of compliance on parasitic motion, and influence of temperature. A special focus is placed on friction and compliance of the mechanical transmission with fault injection and temperature dependence. Aileron actuation is used to highlight the proposals for control design, energy consumption and thermal analysis, power network pollution analysis and fault response.

* Corresponding author at: School of Mechanical Engineering and Automation, Beihang University, Beijing 100083, China.
E-mail addresses: fujianbuaa@126.com (F. Jian), jean-charles.mare@insa-toulouse.fr (J.-C. Maré), fuyongling@126.com (F. Yongling).

Peer review under responsibility of Editorial Committee of CJA.

ELSEVIER **Production and hosting by Elsevier**

http://dx.doi.org/10.1016/j.cja.2016.07.006

1. Introduction

In recent years, increases in fuel costs, a focus on reduced carbon footprint and the emergence of new competitors have driven the aerospace industry to take steps towards creating greener, safer and cheaper air transport.[1] The concepts based on extended use of electricity in "More Electric Aircraft" (MEA) and "All Electric Aircraft" (AEA) have logically defined the technological shift towards greening aviation operations.[2,3] Currently, numerous research activities strive to widen the use of electrical power networks for electrically supplied power users (Power-by-Wire or PbW) as a replacement of conventional hydraulic, pneumatic and mechanical power networks.[4] At the same time, PbW actuators have become sufficiently mature to be introduced in the latest commercial programmes:

- Electro-hydrostatic actuators (EHAs) as backup actuators for primary and secondary flight controls in the Airbus A380/A400M/A350.
- Electromechanical actuators (EMAs) as frontline actuators for several secondary flight controls and landing gear braking in the Boeing B787.

Although they remove central hydraulic power distribution, EHAs still use hydraulics locally to maintain the major advantages of conventional actuators with regard to secondary functions (e.g. back-driving, overload protection, and damping) and in response to failure (i.e. easy hydraulic declutch and extremely low risk of jamming). EMAs, however, remove both central and local hydraulic circuits by transmitting motor power to the load through mechanical reducers (e.g. gearbox, nut-screw). Nevertheless, EMAs are not yet sufficiently mature to replace conventional hydraulic servo-actuators (HSA) in normal mode for safety-critical functions such as flight controls. Several technical challenges still need to be overcome: weight and size constraints for integration, voltage spikes and current transients affecting the pollution and stability of electrical networks, heat rejection for actuator thermal balance, reduced reflected inertia for dynamic performance, increased service life and fault tolerance or resistance (e.g. for jamming or free-run) for safety.[5,6]

A model-based and simulation-driven approach can unquestionably provide engineers with efficient means to address all these critical issues as a whole. In particular, it facilitates and accelerates the assessment of innovative architectures and concepts,[7,8] and their technological embodiments. Introducing all or more electrical actuation raises new challenges:

(a) Heat rejection - the temperature of motor windings and power electronics is a key element affecting service life and reliability. Thus, thermal balance is an important issue in PbW actuators. Unlike in HSAs, where the energy losses is taken away by fluid returning to the reservoir, the heat in PbW actuators has to be dissipated locally into surroundings or a heat sink. Simulation of lumped parameter models can provide a detailed view of the temperature and heat flow fields.[9,10] Unfortunately, these methods are too time-consuming for modelling and simulation at the system-level. In addition, they cannot be used in the early design phases because they are too detailed and require numerous parameters that are not yet known. The heat generated in EMAs comes from a multiplicity of sources: electronic (switching and conduction losses), electrical (copper losses), magnetic (iron losses) and mechanical (friction losses). Accurately quantifying this heat during a reference flight cycle helps determine the operating temperature of the actuator components.

(b) Response to failure - safety-critical functions like primary flight controls must have extremely low failure rates (e.g. 10^{-9} per flight hour). This is achieved through installation of multiple channels for redundancy. However, each channel must have fail-safes to enable the remaining channels to operate correctly. This requirement introduces another challenge in EMAs, where jamming and free-run faults of mechanical components are considered. In HSAs, a fail-safe response to failure (free, damped or frozen) is easily obtained at low mass and low cost by resorting to bypass valves, restrictors, pilot operated check valves or isolation valves. Unfortunately, it is no longer possible to transpose the needs in the hydraulic domain to EMAs where clutches, brakes, dampers and torque limiters may be required. Virtual prototyping at the system-level therefore becomes a focus, not only to support conceptual design but also to verify control and reconfiguration strategies.

(c) Electrical pollution: the power control of electrical machines (e.g. actuator motor) is based on high frequency on/off switching (e.g. 8–16 kHz) of power semi-conductors through pulse width modulation (PWM). Although power is controlled with very low energy losses, it generates high transients in the electrical supply bus and can affect the stability of the electrical network. Moreover, regenerative currents need to be managed properly under aiding-load conditions. This is another reason why model-based systems engineering (MBSE) of PbW actuators calls for more realistic models.

All these considerations support developing high fidelity models with a transverse view of the physical domains involved in EMAs. These models have to be properly structured in order to support the MBSE development process and the associated engineering needs: they must be energy balanced, replaceable and incremental. This paper reports research that has contributed to this goal. It makes wide use of the Bond-Graph methodology for graphical and qualitative modelling. Bond-Graph modelling[11,12] explicitly displays multidisciplinary energy transfers, and the structure and calculation scheme for simulations. Incidentally, it facilitates the design of a model structure that enables incremental or even decremental modelling. In the following sections, the models are developed at a system-level to support various major engineering tasks such as control design, component sizing, thermal management, power budget and network stability for flight control EMAs. Their main contribution concerns model decomposition versus EMA architecture from a multidisciplinary point of view and with special consideration of power flows and response to failure.

Section 2 describes the EMA under study, focusing on power and signal architecture, coupled physical effects and power flows. In Section 3, the EMA power components are modelled with the support of Bond-Graph formalism, paying particular attention to the various sources of energy loss. Section 4 illustrates how the modelling proposals can be implemented in a commercial simulation environment with the example of aileron actuation. In Section 5, the implemented model is simulated in order to highlight its interest for various engineering activities. Finally, the conclusion summarizes the main advances and indicates plans for future work.

2. EMA system description

This study deals with a direct-drive linear EMA. In such an "in-line" EMA, the motor rotor is integrated with the rotating part of the nut-screw. The absence of gear reduction saves weight and offers a high potential for geometrical integration. This design is attractive for aerospace applications because the actuator is compact and easily integrated within the air-frame when the available geometrical envelope is limited. Such an EMA is shown schematically by Fig. 1. When it is applied to flight controls, the load is the flight control surface to which the aerodynamic forces apply. This scheme can also address landing gear actuation applications. In this case, the load is the landing gear leg for extension/retraction or the turning tube for steering.

2.1. Basic components

In this paper, the flight control EMA actuation system consists of the following components:

- actuator control electronics (ACE), which perform closed loop position control
- power drive electronics (PDE), which control the amount of power flowing between the electrical supply and the motor
- an electric motor (DC or 3-phase BLDC/PMSM) that transforms power between the electrical and the mechanical rotational domains
- a nut-screw (NS) mechanical transmission that transforms power between the high speed/low torque rotational and the low velocity/high force translational domains
- sensors of current, speed, position and force if necessary
- a flight control surface, which transforms power between rod translation and surface rotation, through a lever arm effect. This surface is acted on by the aerodynamic forces.

2.2. Control structure

The EMA is position servo controlled. It follows pilot or autopilot demands (pursuit) and rejects the disturbance (rejection) that is generated by the air load. The common way to control the EMA is to use a cascade structure that involves three nested loops: the current (inner) loop, the velocity (middle) loop and the position (outer) loop. If needed, a force sensor can be inserted between the EMA rod and the flight control surface in order to meet the rejection performance requirements through additional force feedback.[13] The controller design is generally based on the linear approach and involves proportional and integral serial correctors. However, particular attention has to be paid to structural compliance and power saturation (voltage and current).[14]

As EMAs naturally include the above-mentioned sensors for the control loop, it becomes possible to develop and implement Health and Usage Monitoring (HUM) functions. In EMAs, different sensors are required to perform the closed-loop position control and protections: motor current and temperature, motor speed, load position and even force to load. The signals delivered by these sensors enable usage monitoring functions to be implemented, without increase in recurrent costs, simply by logging (e.g. peak and mean values). For the same reason, HUM functions can be implemented at a reduced cost: diagnostics detect abnormal levels and determine a faulty device according to its fault signature; prognostics predict the remaining life before a fault generates a failure. HUM is currently investigated for two reasons. First, by enabling on-condition maintenance instead of scheduled maintenance, it contributes to cut operating costs. Second, it is looked at as an attractive means to deal with reliability issues regarding jamming. Although a lot of research effort has been placed on health monitoring of the PDE and EM, robust solutions for health monitoring of the MPT are still at a very low level of maturity. The proposed model of MPT with jamming/free-run/backlash fault injection provides the designers with a significant added value. It allows the assessment of health monitoring algorithms through virtual prototyping since the effect of faults can be observed without intrusive or destructive effects on real hardware. Therefore, the actuator control electronics (ACE) is also in charge of running the HUM algorithms and reporting the EMA faults to the flight control computers (FCCs).

An overview of an EMA control structure is shown in Fig. 2, where signal and power flows are explicitly differentiated. X_c is

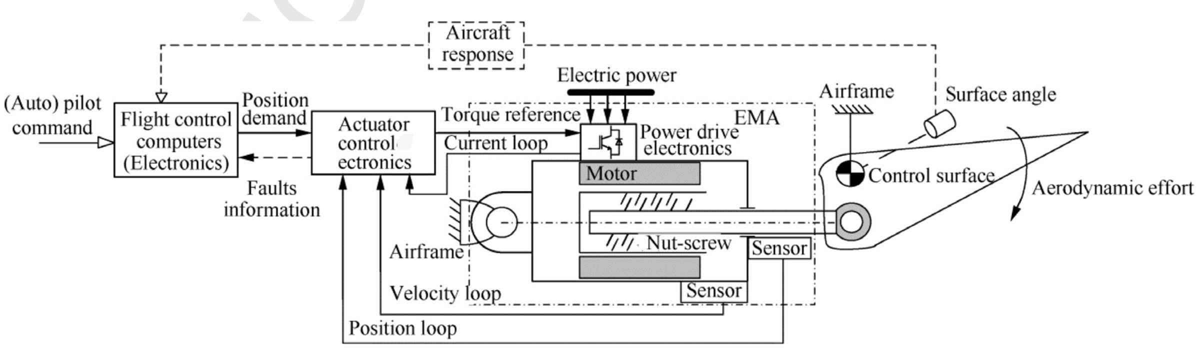

Fig. 1 Schematic of a flight control EMA actuation system.

Please cite this article in press as: Jian F et al. Modelling and simulation of flight control electromechanical actuators with special focus on model architecting, multidisciplinary effects and power flows, *Chin J Aeronaut* (2016), http://dx.doi.org/10.1016/j.cja.2016.07.006

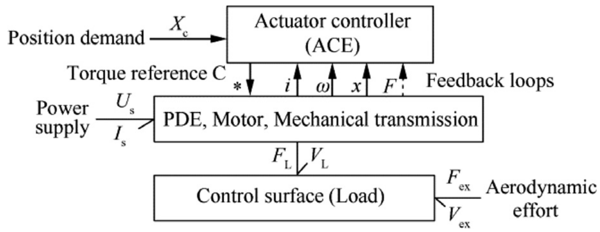

Fig. 2 Synoptic control structure of an EMA system.

the position command (m), C^* is the torque reference for motor control (N·m), the U_s and I_s are the voltage (V) and current (A) of the electric supply, respectively. F_L and V_L are the force (N) and velocity (m/s) from EMA to drive the load, respectively. F_{ex} and V_{ex} are the disturbance of aerodynamic force (N) and velocity (m/s), respectively. The i, ω, x, F are the current (A), rotational velocity (rad/s), position (m), force (N) feedback loops variables, respectively.

According to Bond-Graph formalism, power flows are represented using a single-barbed arrow that carries the two power variables (e.g. voltage and current, force and velocity). Full arrows indicate a signal flow that carries only one type of information. Typically, the EMA is position servo-controlled. Usually, position feedback involves a linear variable displacement transducer (LVDT) that measures rod extension. The load angular position is used for monitoring purposes. The motor angular position and velocity can be measured by an integrated resolver (sinusoidal commutation) or by Hall sensors (triangular modulation).

2.3. Multidisciplinary domain coupling

Designing an EMA system requires multidisciplinary approaches for preliminary power sizing and estimation of the mass and geometrical envelope. Unlike an HSA, an EMA generates heat by energy losses, which has to be dissipated or stored at the actuator level (except in very specific applications where the actuator can be cooled by a dedicated liquid circuit). Energy is lost in transistor switching (commutation losses), the electrical resistance of wires/windings and power electronics (copper and conduction losses), eddy currents and magnetic hysteresis (iron losses) in the motor, and friction losses between moving bodies. Most of these losses govern the thermal balance of an EMA and are sensitive to temperature. This generates a strong multidisciplinary coupling among physical domains, as depicted by Fig. 3. Θ is the temperature (°C), $\dot{S}$ is entropy flow rate (J/K) and the Θ_e Θ_c Θ_i Θ_f and $\dot{S}_e, \dot{S}_c, \dot{S}_i, \dot{S}_f$ are the temperatures and entropy flow rates of the conduction, copper, iron and friction loss, respectively.

2.4. Functional power flows

In a direct-drive in-line EMA, there are two functional types of motion on the same axis: rotation of the motor rotor and translation of the nut-screw rod. In order to increase the fidelity of the EMA, these two degrees of motion should be considered for any of its components. This enables the rod anti-rotation function and the rotor axial thrust bearing functions to be modelled. In this way, it is possible to consider

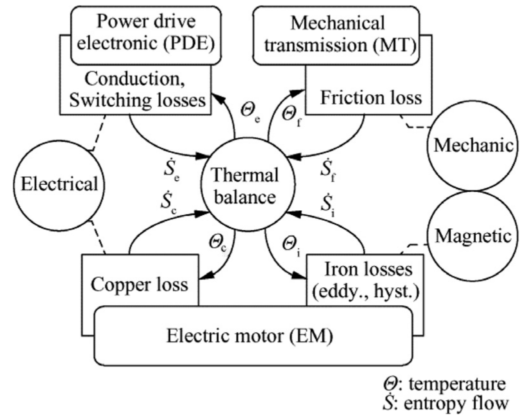

Fig. 3 Multi-domain coupling of an EMA for thermal balance.

imperfect bearings (e.g. compliance and friction) and access the reaction forces, e.g. the force and torque at the interface between the EMA housing and the airframe. A second key idea for structuring the EMA model consists of keeping the same topology as the cut-view of the EMA. These two principles are illustrated in Fig. 4. The C and ω are power flows of torque (N·m) and rotational velocity (rad/s) for mechanical rotational motion, respectively. The F and V are the power flows of force (N) and velocity (m/s) for mechanical translational motion. The torque and C_m are the motor shaft torque (N·m), ω_m is the motor rotor velocity (rad/s), ω_r is the relative rotation velocity in the mechanical power transmission system (rad/s), F_t and V_t are the MPT output force (N) and velocity (m/s). U_m and I_m are the voltage (V) and current of motor electric supply, respectively.

It is important to note that the proposed model architecture also enables the thermal flows to appear explicitly. In the figure, only one thermal body is considered that receives the heat generated from power losses and exchanges it with the surroundings. However, the model structure enables individual thermal bodies to be considered for each component or zone of the EMA.[10] The detailed modelling of power flows is addressed in Section 3.6.

2.5. Model architectures V.S. engineering needs

At the system-level of EMA modelling and simulation, the model depends strongly on the needs of the current engineering task; the best model is never the most detailed one. For this reason, it is particularly important to properly select the physical effects to be considered in order to get the right level of model complexity. Typically, the EMA model can be developed for simulation aided conceptual design (architectures and function), control design, thermal balance, mean and peak power drawn. Since the level of detail is not obviously identical for each component, the EMA should be decomposed into three package models: power drive electronics (PDE), electric motor (EM) and mechanical power transmission (MPT). Table 1 links the engineering tasks to the physical effects to be considered following the proposed decomposition.

This approach requires the components' models to be made replaceable, whether each physical effect is considered or not. In the well-established simulation environments, this raises causality issues that are addressed in Section 4.

Please cite this article in press as: Jian F et al. Modelling and simulation of flight control electromechanical actuators with special focus on model architecting, multidisciplinary effects and power flows, *Chin J Aeronaut* (2016), http://dx.doi.org/10.1016/j.cja.2016.07.006

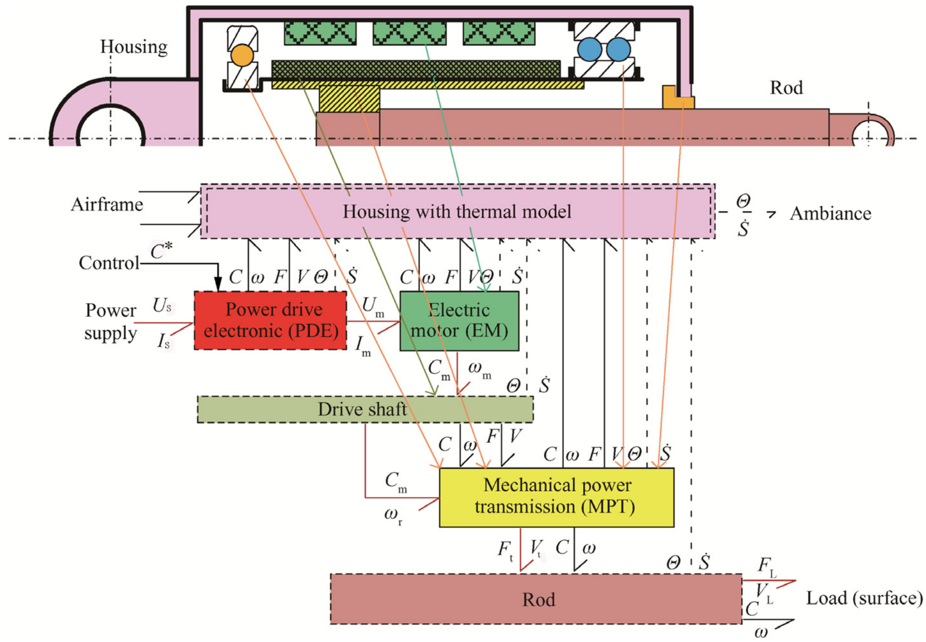

Fig. 4 Functional architecture of EMA model topology with power flows.

Table 1 Model architecture vs. engineering needs.

Model architecture	Engineering needs								
	Functional	Power sizing	Thermal balance	Natural dynamics	Stability accuracy	Consumed energy	Failure response	Load propagation	Reliability
PDE									
Perfect transformer	Y	Y	Y	Y	Y	Y	Y	Y	Y
Dynamic function	Y	N/A	N/A	P	Y	N/A	N/A	N/A	N/A
With power loss	N/A	Y	Y	N/A	N/A	Y	P	N/A	N/A
EM									
Perfect converter	Y	Y	Y	Y	Y	Y	Y	Y	Y
With power loss	N/A	Y	Y	Y	Y	Y	N/A	N/A	N/A
Advanced model	N/A	Y	Y	P	P	Y	N/A	P	N/A
MPT									
Perfect transformer	Y	Y	Y	Y	Y	Y	Y	Y	Y
With friction loss	N/A	Y	Y	Y	Y	Y	Y	P	P
With compliance	N/A	P	N/A	P	P	N/A	P	P	P
With fault	N/A	N/A	N/A	N/A	P	N/A	Y	N/A	Y

Note: Y means yes; P means possibly but depends on relative level; N/A means not applicable.

3. System-level modelling of physical effects

The physical effects in EMA are complex and multi-domain: electric, magnetic, mechanical and thermal. Energy balanced modelling is considered an imperative requirement here because of its importance for assessing coupled thermal effects. This is why Bond-Graph formalism particularly suits the first step of model structure definition. The second step includes re-using (or adapting) models from the standard libraries of commercial simulation software in order to save time and reduce risk (models are assumed to have been tested, validated, documented, and supported and be numerically robust).

3.1. Power drive electronics (PDE)

The function of the power drive electronics is to modulate the power transferred between the supply bus and the motor by actions on the motor winding voltages according to the switching signals sent to the power transistors. Consequently, the PDE can be seen as a perfect power transformer in which power losses come from switching and electrical resistance.

3.1.1. Perfect transformer

Functionally, the PDE operates as a perfect modulated power transformer, an MTF in the Bond-Graph, between the electric power supply and motor windings. It is driven by the actuator controller, the pulse width modulation function of which outputs the duty cycle α, $\alpha \in [-1;1]$

$$\begin{cases} U_m = \alpha U_s \\ I_m = I_s/\alpha \end{cases} \tag{1}$$

3.1.2. Dynamics of the torque control

For preliminary design of controllers, it may be advantageous to develop a simplified model that merges the PDE and the motor: the motor current I_m is linked to the motor electromagnetic torque C_r through the motor torque constant K_m and the dynamics of the current loop, which is modelled as an equivalent second order model. Therefore, the electromagnetic torque can be calculated as

$$C_r = \frac{\omega_i^2}{s^2 + 2\xi_i\omega_i s + \omega_i^2} C^* \tag{2}$$

where s is the Laplace variable, and the two parameters $\omega_i = 2\pi f_i$ and ξ_i are the current (torque) loop natural frequency (rad/s) and the dimensionless damping factor, respectively. These parameters can be provided by the PDE supplier (typically f_i is in the range 600–800 Hz while ξ_i is in the range 0.6–1).

It is important to note that this model implicitly assumes that the current loop perfectly rejects the disturbance coming from the motor back electromotive force (BEMF). In practice, torque response to torque demand requires a more complex model, including the structure of the controller (e.g. PI control plus BEMF compensation), noise filtering, sampling effects, parameter variation under temperature, and Park transformation for 3-phase electric motors. Some of these effects are introduced into the model implemented in Section 4.3.1. There are no special issues raised by adding the remaining effects.

3.1.3. Conduction losses

In most chopper and inverter bridge circuits, the basic commutation cell involves a solid-state switch (e.g. IGBT) and a diode that serves for free-wheeling by an anti-parallel structure. These components generate energy losses, the R effect in the Bond-Graph, which can be divided into three types: on-state conduction losses, off-state blocking (leakage) losses, and turn-on/turn-off switching losses.[15]

In practice, the off-state blocking losses can be neglected because leakage currents are extremely low.[15] When a power transistor or a diode conducts, it generates a voltage drop that is given in its datasheet as a current/voltage characteristic.[16] This characteristic can be modelled by combining an on-state zero-current forward threshold voltage U_{th} (V) and an internal resistance R_{on} (Ω). Consequently the voltage drop U_d (V) is expressed versus the root mean square (RMS) current I_{drms} (A)

$$U_d = U_{th} + R_{on} I_{drms} \tag{3}$$

and the associated average power loss P_d (W) is as follows:

$$P_d = U_d I_{drms} \tag{4}$$

For example, the conduction loss P_d of the IGBT mentioned in Table 4 at rated current is 88.3 W. This corresponds to 2.6% of the rated power. At rated output power, the efficiency of the power switch is therefore 97.4% when only conduction loss is considered.

3.1.4. Switching losses

At each switching, a phase lag occurs between current and voltage within the electronic component. This induces a very small energy loss at turn-on E_{on} (J) and at turn-off E_{off} (J). However, the resulting power loss cannot be neglected when the switching frequency f_{sw} (Hz) is high (typically in the range of 10 kHz for aerospace EMAs). This effect can be viewed as a current leak I_{sw} (A) that is directly proportional to the switching frequency

$$I_{sw} = \frac{E_{sw} f_{sw}}{U_s} = \frac{(E_{on} + E_{off}) f_{sw}}{U_s} \tag{5}$$

Therefore, the switching power loss P_{sw} (W) is

$$P_{sw} = (E_{on} + E_{off}) f_{sw} \tag{6}$$

To illustrate the order of magnitude, the IGBT mentioned in Table 4 produces a switching loss P_{sw} of 106.4 W, when f_{sw} is 8 kHz. This represents 3.1% of the rated power. When combined with the conduction loss at rated current, the overall efficiency of the IGBTs (electric power delivered to motor/consumed electric power) is 94.3%.

At this level, it is important to keep in mind that the effective values of R_{on}, U_{th}, E_{on} and E_{off} depend on the temperature of the junction. This may cause a snowball effect. In practice, there is no problem in reproducing this dependency in the model through a look-up table or a parametric model as long as the temperature is available as an input of the model.

3.2. Electric motor (EM)

At system-level, the electric motor can be seen as a perfect power transformer in which the torque balance

$$C_m = C_{em} - C_j - C_d - C_{cg} \tag{7}$$

where C_{em} is the electromagnetic torque (N·m), C_j is inertial torque (N·m), C_d is the dissipative torque (N·m) and C_{cg} is the compliance torque (N·m).

3.2.1. Perfect power converter

The electric motor is an electromechanical power transformer that functionally links current to torque and voltage to velocity (a gyrator GY in the Bond-Graph)

$$\begin{cases} C_{em} = K_m I_m \\ \omega_m = U_m/K_m \end{cases} \tag{8}$$

where K_m is the motor electromagnetic constant (N·m/A).

3.2.2. Inertial effect

The rotor inertia J_m (kg m^2), an inertance I element in the Bond-Graph, generates an inertial torque

$$C_j = J_m \frac{d\omega_m}{dt} \tag{9}$$

Attention must be paid to the fact that the inertial torque involves the absolute velocity of the rotor, which is a time derivative with respect to the earth frame of reference. The inertial torque cannot be neglected for three reasons. Firstly, in very demanding applications, e.g. fighter aircraft or space launchers, the inertial torque takes the major part of the electromagnetic torque during transients (high rate of acceleration or deceleration). Secondly, under aiding load conditions, it impacts the transient back-drivability of the actuator by opposing torque to the load acceleration. Lastly, the kinetic energy stored by the inertial effect must be absorbed when the end-stops are reached in such a way as not to generate excessive force. For example, EMAs reflect a huge inertia at the load level, typically 10–20 times greater than the load itself. Conversely, HSAs only reflect a few per cent of the load inertia.[14,17]

3.2.3. Dissipative effects

Energy dissipation, modelled by R elements in a Bond-Graph, comes from copper, iron and friction losses.

(1) Electric domain: Copper loss - The primary power loss in the electric domain of a motor (also called Joule loss). Copper loss comes from the voltage drop U_{co} (V) in motor windings due to their resistance R_s (Ω) to a current I_s (A)

$$U_{co} = I_s R_s \tag{10}$$

The associated power loss P_{co} (W) is given by

$$P_{co} = U_{co} I_s = R_s I_s^2 \tag{11}$$

For example, the copper loss P_{co} of the motor mentioned in Table 4 at rated current is 194.4 W. This represents 5.6% of the rated output power. The associated efficiency is 94.4%.

(2) Magnetic domain: Iron loss - The variation of the flux density in the magnetic circuit of the motor generates eddy current and hysteresis losses. The reversing magnetic field in iron induces a voltage that produces eddy currents due to the electrical resistance of iron. As there is no access to the magnetic quantities during measurements, the effect of eddy currents is commonly expressed as an equivalent power loss. This power loss P_{ed} (W) is modelled by the first member of the Steinmetz equation[18] as a function of the eddy current constant k_{ed}, the magnetic flux density B_s (T) and the velocity ω_m

$$P_{ed} = k_{ed} B_s^2 \omega_m^2 \tag{12}$$

As a result, the torque loss C_{ed} (N·m) due to eddy currents takes the form of an equivalent viscous friction torque that is given by

$$C_{ed} = k_{ed} B_s^2 \omega_m \tag{13}$$

Magnetic hysteresis appears within ferromagnetic materials between the remanence flux density and the coercivity (*B-H* curve). The area of the hysteresis domains represents the work done (per unit volume of material). For each cycle, the magnetic hysteresis generates an energy loss that depends directly on the motor electrical frequency. The hysteresis power loss P_{hy} (W) can be modelled using the second member of the Steinmetz equation[18] that links the hysteresis constant k_{hy} and the magnetic flux density B_s

$$P_{hy} = k_{hy} B_s^{\gamma} \omega_m \tag{14}$$

where γ is the Steinmetz constant, typically in the range 1.5–2.5.
According to Eq. (14), the hysteresis effect can be modelled globally as pure Coulomb friction

$$C_{hy} = k_{hy} B_s^{\gamma} \tag{15}$$

To illustrate the order of magnitude, when the motor mentioned in Table 4 operates at the maximum velocity ω_{max} of 314 rad/s (3000 r/min), the power loss P_{ed} by eddy current is 14.7 W and the hysteresis loss P_{hy} is 29.1 W. These effects represent 1.2% of the rated output power of the motor.
If a more detailed description is required, hysteresis has to be modelled as a function of the instantaneous magnetic field, e.g. by using switched differential equations.[19]

(3) Mechanical domain: Friction loss - Power loss P_{fm} (W) in a motor comes from friction at bearings and drag due to shear within the rotor/stator air gap. The friction torque generated by the hinge bearing is addressed in the next section. The drag friction torque can be modelled as proposed in Ref. 20

3.2.4. Capacitive effect

The variation of the air gap permeance of the stator teeth and slots above the magnets during rotor rotation generates a torque ripple[21]: the cogging (or detent) torque. This is an energy storage effect that is equivalent to a spring effect, a C element in Bond-Graph. Modelling the cogging effect may be important for two reasons. The cogging torque can be used in some applications as a functional effect to avoid back-drivability. Also, as cogging generates a torque ripple, the frequency of which depends on the relative velocity of the rotor, it may excite the natural dynamics of EMAs and its mechanical environment, potentially leading to vibrations and noise emission.

A system-level representative model of cogging torque C_{cg} can be expressed versus rotor/stator relative angle θ_m (rad). It is parameterized by the number n_p of motor pole pairs and by the cogging torque factor λ at motor rated torque C_n (N·m)[18]

$$C_{cg} = \lambda C_n \sin(n_p \theta_m) \tag{16}$$

The maximum cogging torque can be reduced to 1% or 2% of the rated torque in today's high performance motors[22] when it appears as a parasitic effect. Cogging torque in the motor mentioned in Table 4 has a maximum magnitude of 0.1 N·m, which represents 1% of the rated motor torque.

3.2.5. Magnetic saturation

At flux densities above the saturation point, the relationship between the current and the magnetic flux in ferromagnetic materials ceases to be linear: a given current generates less magnetic flux than expected, as illustrated by the magnetization curve given in Fig. 5. Consequently, the motor constant drops in the saturation domain. In addition, the inductance of motor windings is also affected by magnetic saturation. Magnetic saturation can therefore be modelled by modulating the motor constant and the windings' inductance as a function of current. For example, the electric motor of an EMA (GSX-40 series) in Ref. 23, the maximum permitted current is twice the steady state current but generates only 30% more than the rated torque. Modelling and simulation of magnetic saturation are well documented in bibliography, e.g. in Refs. 24,25

3.3. Mechanical power transmission (MPT)

The mechanical transmission appears as a rotary to linear power transformer, a TF element in Bond-Graphs. In direct-drive linear EMAs, this transformation is obtained by using a nut-screw. For lumped parameter modelling purposes, the real nut-screw can be decomposed into three parts, as shown in Fig. 6: a perfect nut-screw, a friction loss and a compliance effect (that can represent preload, backlash or pure compliance). In the proposed EMA model architecture, the bearings, joints and end-stop are not explicitly considered to be part of the nut-screw model. Consequently the nut-screw model involves 4 mechanical power ports (rotation and translation of nut and screw). An additional heat port enables the nut-screw model to output the heat generated by its power losses. This port also gives temperature to the nut-screw model in order to reproduce its influence on friction and compliance. The order or decomposition has been chosen according to the engineering needs.[26]

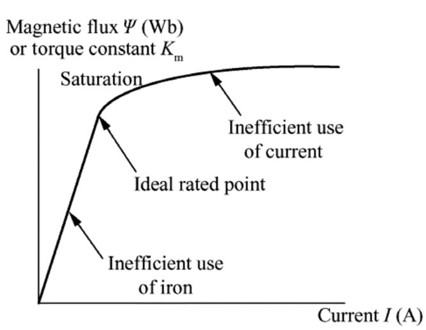

Fig. 5 Magnetic saturation effects on an electric motor.

3.3.1. Perfect transformer

When the nut-screw is considered perfect, it achieves pure power transformation between the electric motor and the load with a ratio $(2\pi/p)$

$$\begin{cases} F_L = \frac{2\pi}{p} C_m \\ V_L = \frac{p}{2\pi} \omega_m \end{cases} \tag{17}$$

where p is the pitch (m) of nut-screw.

3.3.2. Friction losses

The friction of the mechanical transmission mainly comes from bearings, joints and the nut-screw. Friction loss is a very complex phenomenon that is highly dependent on velocity, external load and temperature. This explains why there are numerous types of friction models.[27,28]

(1) Velocity dependent - From the control designer's point of view, the LuGre model is an accurate model of velocity-friction characteristics that has capability to capture static and dynamic friction behaviours.[29] However, for a preliminary control study, the friction is always modelled as a pure viscous effect that makes the friction force proportional to the sliding velocity. This gives

$$F_f = f_e v_r \tag{18}$$

where F_f is the nut-screw pure viscous friction force (N), f_e is the coefficient of viscous friction (N/(m/s)), and v_r is the relative velocity (m/s) of nut-screw.

(2) Velocity and load dependence - Friction can be represented in a more realistic way by introducing its dependence on load. For a nut-screw, a five parameter model, Eq. (19), has been identified from experiments for nut-screws by Karam.[30] It introduces a constant Coulomb friction (first part), a Stribeck effect (second part) and a load and power quadrant dependent Coulomb effect (last part):

$$F_f = [F_{cl} + F_{st} e^{-|v_r|/v_{st}} + |F_L|(a + b\,\mathrm{sgn}(F_L v_r))]\mathrm{sgn}(v_r) \tag{19}$$

where F_{cl} and F_{st} respectively are the Coulomb force and the Stribeck force (N), v_{st} is the Stribeck reference velocity (m/s), a is the mean coefficient of external force and b is the quadrant coefficient.

(3) Load dependent and load independent - In this approach, friction is decomposed into load dependent and load independent components.[16] This model is con-

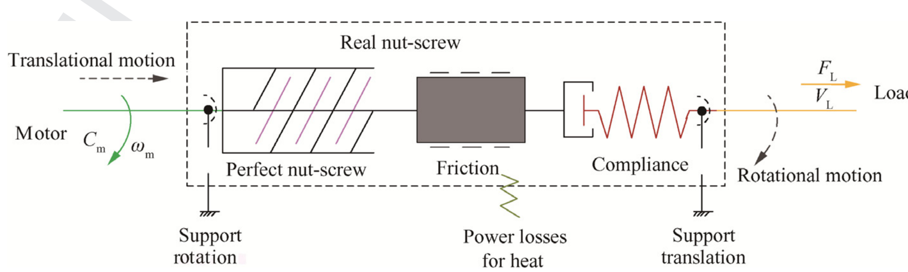

Fig. 6 Proposed model of the MPT.

sistent with nut-screw suppliers' datasheets, which provide efficiency (the load dependent friction), as well as the no-load friction under opposite load and the no-drive friction under aiding load (the load independent friction). The velocity effect is added in a second step by introducing its influence on these parameters. The details of this modelling approach have been presented in Ref. 28

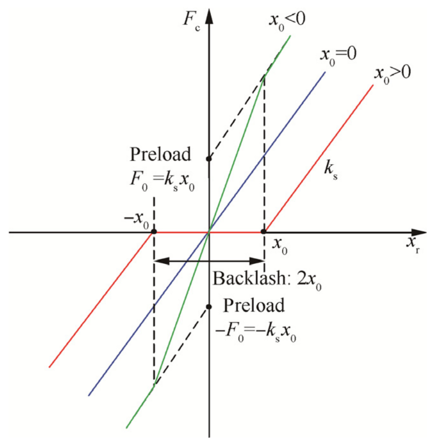

Fig. 7 Compliance model with backlash and preload.

Both types of models are able to reproduce the load effect that is the main contributor to friction in mechanical transmissions like a nut-screw. For any friction model for mechanical transmission, the power loss P_{tf} (W) is calculated as

$$P_{tf} = F_f v_r \tag{20}$$

3.3.3. Compliance effect

Obtaining a realistic model of compliance is of particular importance because compliance significantly impacts the dynamic performance[14] and the service life of the EMAs. Within EMAs, the mechanical transmission is not infinitely rigid. This makes it compliant due to the elastic deformation of solids under mechanical and thermal stress, in particular at contact locations. In the absence of preload and backlash, the axial mechanical stiffness decreases around the null transmitted force where not all the contacts are fully loaded. This generates the so-called lost motion. When they exist, backlash or preload can also be considered as a compliance effect, a C element in Bond-Graphs, because they algebraically link force and relative motion, as elasticity does (see Fig. 7). F_c is the elastic force (N), F_0 is the preloading force (N), k_s is the stiffness (N/m), x_r is the relative displacement (m), x_0 is a proposed single parameter (m) and can be used to reproduce backlash as well as preload in the compliance model.

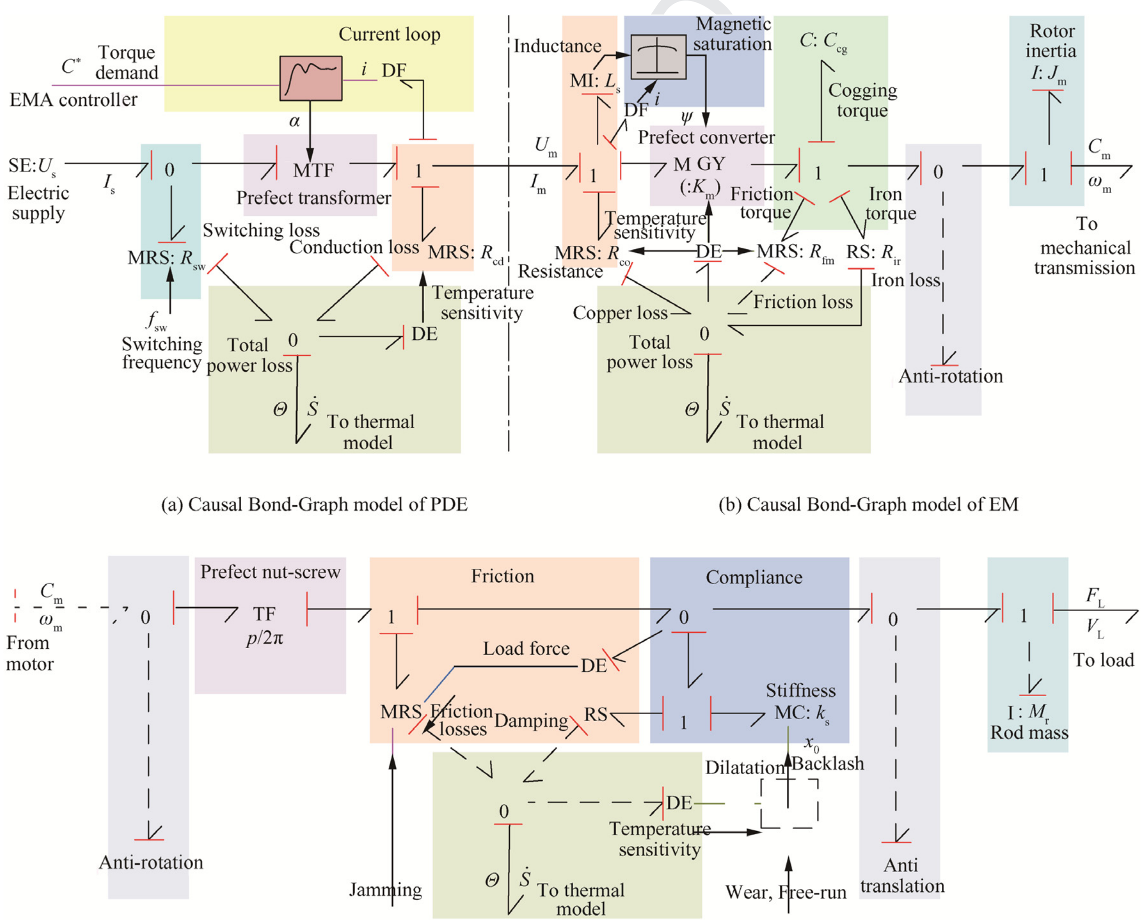

(c) Causal Bond-Graph model of MPT

Fig. 8 Causal Bond-Graph modelling of the EMA.

(1) using $x_0 = 0$ models a pure spring effect. The elastic force F_c is purely proportional to the x_r, and can be given by

$$F_c = k_s x_r \tag{21}$$

(2) using $x_0 > 0$ models a backlash effect. It displays a total dead-zone of $2x_0$ and the elastic force F_c is

$$F_c = \begin{cases} k_s(x_r - x_0) & x_r > x_0 \\ 0 & |x_r| \leqslant x_0 \\ k_s(x_r + x_0) & x_r < -x_0 \end{cases} \tag{22}$$

(3) using $x_0 < 0$ models a preload effect. The preload force is $|F_0| = k_s|x_0|$ and the elastic force F_c is

$$F_c = \begin{cases} k_s(x_r - x_0) & x_r > -x_0 \\ 2k_s x_r & |x_r| \leqslant |x_0| \\ k_s(x_r + x_0) & x_r < x_0 \end{cases} \tag{23}$$

For numerical stability and rapidity, the compliance model is implemented by combining Eqs. (21)–(23) in such a way as to avoid switches or "if" functions. The elastic force F_c can be expressed as

$$F_c = k_s\left\{x_r - \frac{x_0}{2}(1 - \text{sign}(|x_0| - |x_r|)\text{sign}(x_r) - \frac{x_r}{2}\text{sign}(x_0)[1 - \text{sign}(|x_r| - |x_0|)]\right\} \tag{24}$$

Although it is low, structural damping must be considered with compliance in order to avoid unrealistic simulated oscillations. As the physical knowledge about it is very poor, structural damping is usually considered as a linear function of the relative velocity and of damping coefficient d_s ($\text{N}\cdot\text{m}^{-1}\cdot\text{s}$)). In order to avoid discontinuities when contact is made or broken, the damping force F_d (N) acting in parallel with the elastic force F_c has to be bounded:

$$F_d = \begin{cases} \min(F_c, d_s v_r) & x_r > x_0 \\ 0 & |x_r| \leqslant x_0 \\ \max(-F_c, d_s v_r) & x_r < -x_0 \end{cases} \tag{25}$$

Therefore, the contact force F_{ct} (N) for MPT compliance is the sum of elastic force F_c and damping force F_d:

$$F_{ct} = F_c + F_d \tag{26}$$

The power loss due to structural damping P_{sd} (W), although negligible in general, can be calculated to make the nut-screw model exactly balanced with respect to energy:

$$P_{sd} = F_d v_r \tag{27}$$

3.4. Modelling of faults

Simulating the response to failure of EMAs is mandatory if flight control systems are to be verified through virtual integration, particularly to assess the merits of health monitoring features or reconfiguration after failure has occurred. The main feared events in the power path of an EMA are summarized by Balaban.[31] Faults of PDE (e.g. open circuit) and of EM (e.g. winding short circuits or demagnetization) are not considered below because they are addressed in numerous publications.[32–34] For this reason, the focus is on major faults that may occur in the mechanical transmission: jamming, increased backlash or reduced preload or free-run. Jamming can be modelled by increasing the friction model parameters in order to force stiction. According to the proposed model of compliance, reduction in preload, augmentation of backlash and even free-run can be modelled by increasing the backlash parameter x_0.

3.5. Sensitivity to temperature

The heat flow generated by internal energy losses makes EMA temperature increase. In turn, temperature impacts the energy losses that affect heat flow. This produces a looped effect that cannot be neglected when the intention is to assess the thermal equilibrium or service life of an EMA. The proposed model architecture involves a thermal port for any component. Consequently, it can easily enable the temperature to be used as a time variable input in the models of energy losses.

3.5.1. Influence on electric parts

The on-state resistances, forward voltage drop and switching loss of IGBTs (diodes and transistors) in PDE and the winding resistances in EM increase when the temperature increases. The effect of temperature is rarely documented in suppliers' datasheets or product catalogues. As the energy loss grows accordingly, it causes a snowball effect. However, in the absence of more accurate data, the forward voltage drop and switching loss can be assumed to linearly depend on temperature, like the electric resistance but by a different temperature coefficient:

$$R_1 = R_0[1 + \varepsilon_R(\Theta_1 - \Theta_0)] \tag{28}$$

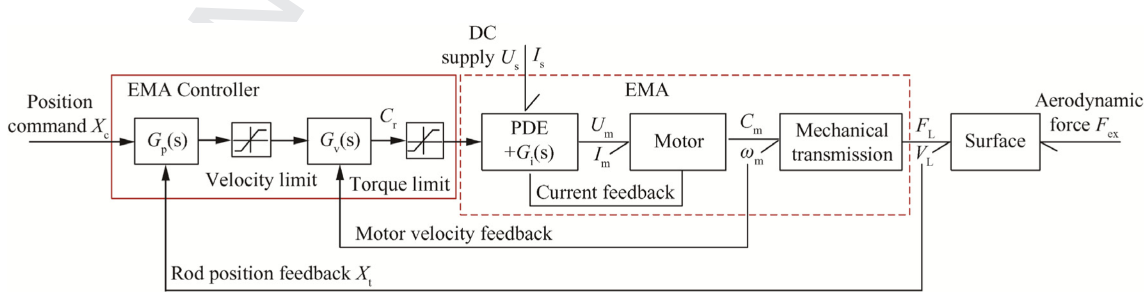

Fig. 9 Schematic of the EMA classical control design.

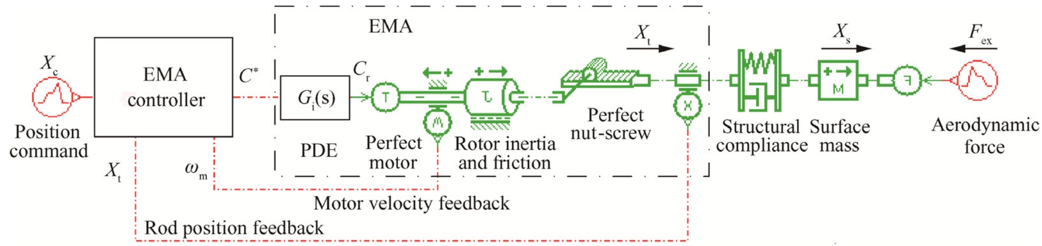

Fig. 10 Basic EMA model for flight surface control in AMESim.

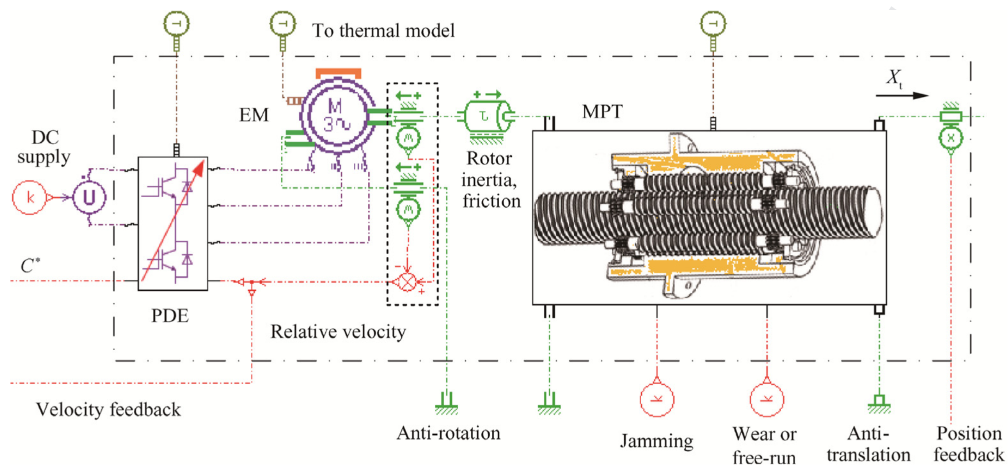

Fig. 11 Realistic EMA model implemented in AMESim.

where R_1 and R_0 are the component resistance (Ω) at actual operating temperature Θ_1 (°C) and at reference temperature Θ_0 (°C) respectively, and ε_t is the temperature dependence coefficient of the material resistance (ε_{Ron} is for the IGBTs "on" resistance and ε_{Rw} is for the stator wingdings resistance). The temperature coefficients of IGBTs forward voltage and switching loss can be respectively introduced by ε_u and ε_s.

3.5.2. *Influence on magnets*

The increase in motor temperature may decrease the performance of magnets, which lowers the K_m. This also can be modelled in a first step as a linear dependency on temperature:

$$K_{m1} = K_m(1 + \varepsilon_m(\Theta_1 - \Theta_0)) \tag{29}$$

where K_{m1} is torque constant (N·m/A) at the actual operating temperature, and ε_m is the negative temperature dependence of the magnetic material. This sensitivities of common magnetic materials are illustrated in Ref. 35

3.5.3. *Influence on friction*

It is well known that friction depends heavily on temperature, represented by $\tilde{F}_f$ (N). Modelling this effect at system-level has been addressed in detail by Maré.[28] A simple approach may consist of using weighting friction as a function of a temperature-dependent factor $\tilde{\mu}_f(\Theta)$ to modify the advanced friction model in Eq. (19).

$$\tilde{F}_f = \tilde{\mu}_f(\Theta)F_f \tag{30}$$

However, it has to be kept in mind that the effect of temperature on friction is poorly documented, including in suppliers' datasheets.

3.5.4. *Influence on dimensions*

Temperature variation causes solids to dilate. This leads to variations in dimension and impact preload, backlash and friction. Once again, if a model of dilation is developed, this effect can be easily introduced using the temperature variable of the heat port. For example, the temperature introduced parameter $\tilde{x}_0$ (m) used to present the temperature sensitivity to x_0 of MPT compliance model, which can be described by using a temperature-dependent factor $\tilde{\mu}_x(\Theta)$.

$$\tilde{x}_0 = \tilde{\mu}_x(\Theta)x_0 \tag{31}$$

This effect can be significantly reduced in design by adequate selection of materials to avoid differential dilation.

3.6. *Causal Bond-Graph model*

All the above-mentioned physical effects can be considered in a causal Bond-Graph model (see Fig. 8). The Bond-Graph is consistent with incremental modelling objectives that facilitate the progressive development of increasingly complex models. As shown in Fig. 4, the EMA model can be split into three parts in order to explicitly display the physical architecture: power drive electronics, electric motor and mechanical transmission. The Bond-Graph model is augmented by causal marks[36] that graphically display the model calculation structure. In this way, it can be verified that the proposed model is consistent with numerical implementation in the commercial simulation software, which still requires algebraic loops and time derivation to be avoided.

The Bond-Graph model of the PDE is shown in Fig. 8(a). The basic element is the perfect and modulated power

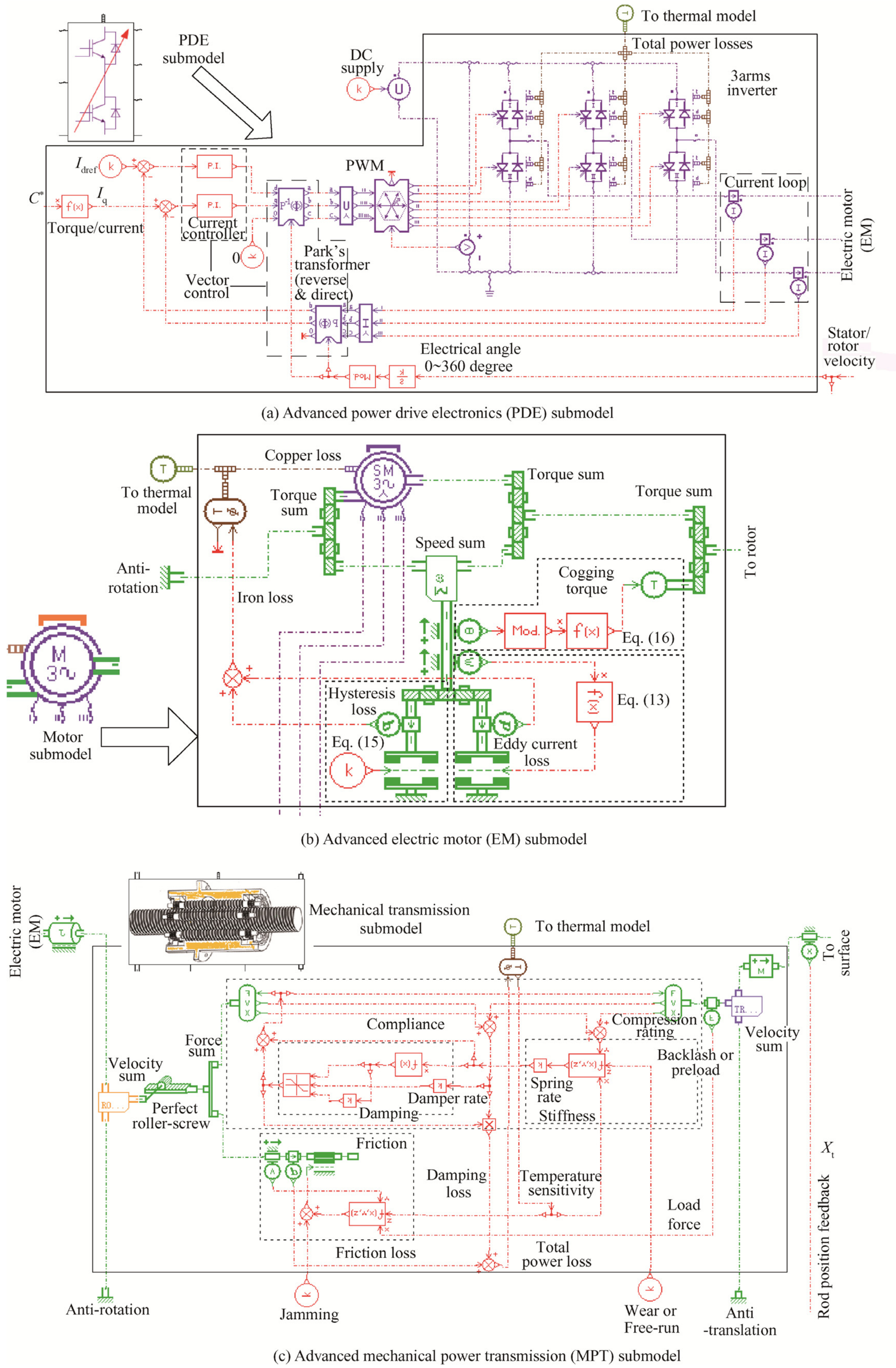

Fig. 12 Advanced supermodels of the EMA in AMESim.

Table 2 EMA controller and load parameters.

Parameter	Value
Position loop proportional gain K_p (rad·s^{-1}·m^{-1})	4500
Velocity loop proportional gain K_v (N·m·s/rad)	0.47
Velocity demand saturation ω_{lim} (rad/s)	314
Torque demand saturation C_{lim} (N·m)	10
Current loop proportional gain K_{ip} (V/A)	67.8
Current loop integral gain K_{ii} (V·ms^{-1}/A)	17.7
Ideal structural stiffness k_t (N/m)	5×10^9
Ideal structural damping d_t (N·s/m)	1×10^4
Common surface reflected mass M_s (kg)	600

Table 3 Motor basic parameters of an EMA.[23]

Parameter	Value
Bus voltage U_m (V)	400
Continuous rating current I_n (A)	6.05
Continuous motor torque C_n (N·m)	9.89
Rated speed ω_n (r/min))	3000
Torque constant K_m (N·m/A)	1.65
Stator resistance R_s (Ω)	1.77
Stator inductance L_s (H)	0.00678
Lead of screw p (mm)	2.54
Rod mass M_r (kg)	1
Mass of magnetic material M_B (kg)	4
Magnetic flux density B_s (T)	2
Rotor inertia J_m (kg·m^2)	0.00171
Number of pole pairs n_p	4

transformer (MTF). The current (or torque) loop can be included as a dynamic function that affects the torque demand. The power losses of conduction and switching can be represented by two dissipative modulated resistor fields (MRS) which link to the thermal port. The switching loss (R_{sw}) is modelled as a leakage current on the power supply side and is fixed by the switching frequency f_{sw} of the PWM. The conduction loss (R_{cd}) is modelled as a voltage drop on the motor side, which is affected by temperature as mentioned in Section 3.5.

The Bond-Graph model of the EM is presented in Fig. 8(b). The element GY corresponds to the perfect power transformation between the electrical and mechanical domains. Global inertia (rotor and screw) and motor friction are modelled as mechanical inertance J and resistance R_{fm}, respectively. The magnetic saturation can potentially be introduced as a modulating signal by its effects on the perfect power transformation between the current in the field windings and the magnetic flux (gyrator GY becomes MGY), where the current is introduced by the flow detector DF element. This can also occur from its effect on the inductance of motor windings (inertance I becomes MI). Copper losses are introduced as a resistance element that generates a voltage drop (1 junction) in the electrical domain. In accordance with the models proposed by Eqs. (13) and (15), iron losses are introduced as the friction loss, so two resistance elements generate torque losses (1 junction) in the mechanical domain. According to Eq. (16), the cogging torque is represented by a nonlinear mechanical capacitance (C_{cg}). Any power loss (electromagnetic, electric and mechanical) adds to the heat flow at the motor heat port. Only one thermal node (0 junction) is considered in order to make the model simple. Consequently all effects are subjected to the temperature that is sensed by the effort detector, DE element. However, if a detailed thermal model of the motor is developed, there is no particular issue connected with splitting the thermal nodes into different parts associated with windings, magnets, housing, etc.

The causal Bond-Graph model of MPT is given in Fig. 8(c). A perfect nut-screw is presented as a modulated power transformer (MTF) that operates on the relative rotational and translational velocities of the nut and screw. For this purpose, two 0 junctions are used to generate these relative velocities in case the support motion has to be considered. Inertial effects can be optionally considered so as to meet the causal constraints imposed by the motor or the load model. The friction loss is presented as a dissipative modulated resistor field (MRS) that links to the thermal port. Structural damping in the compliance model is introduced with a resistor field (RS) that also links to the thermal port. The temperature imposed on these RS fields enables the friction losses to be easily made sensitive to this variable. In addition, an effort detector (De) is introduced to obtain the temperature variable for the dilatation model that is ready for implementation within the compliance sub-model. Jamming can be forced by increasing the load independent force that affects the friction loss. A reduction in the preload or an increase in backlash/free-run can also be introduced to model wear or faults by increasing the compliance parameter x_0.

4. Virtual prototype and model implementation

The former sections presented the EMA model architecture and multidisciplinary effects that are highly nonlinear. Therefore, analytical studies are no longer adequate and numerical simulation becomes mandatory for assessing architectures and analysing power flows. In this section, a virtual prototype model of a flight control EMA system is built in the multi-domain system-level simulation, AMESim, environment. The available libraries offer validated submodels and expert management of integration solvers to give accurate and robust simulation. Re-using the as many available sub-models as possible is an efficient solution that enables the engineer to concentrate on design and not on detailed model making or even on numerical issues. The following sections illustrate how the proposed model architecture and structure enable incremental modelling of the power elements of the EMA during the different phases of development. For this reason, no specific attention is paid to advanced control. The effects of digital control (sampling, quantization and computer time cost) and measurements (sensors, signal conditioning and filtering) are not considered, though they can be introduced easily as reported in Ref. 37

4.1. Control structure

The block-diagram of the EMA control structure under study is shown in Fig. 9. The PDE is a four-quadrant three-phase inverter, and the motor is of the PMSM type. The motor rotor is rigidly connected to the nut of an inverted roller-screw. The flight control surface, not part of the EMA model, is simply modelled as an equivalent translating mass to which the air

Please cite this article in press as: Jian F et al. Modelling and simulation of flight control electromechanical actuators with special focus on model architecting, multidisciplinary effects and power flows, *Chin J Aeronaut* (2016), http://dx.doi.org/10.1016/j.cja.2016.07.006

Table 4 Advanced parameters of an EMA model.[23,40,41,18,42]

EMA devices	Parameter	Value	Source
Power Drive Electronics (PDE) (Conduction and switching losses)	DC supply voltage U_s (V)	565	Test bench installation datasheets[23] and setting
	PWM frequency f_{sw} (Hz)	8000	
	Transistor resistance in "on" state R_{ton} (Ω)	0.036	Referenced from IGBT datasheets[40, 41]
	Transistor forward voltage drop U_{tth} (V)	0.9	
	Diode "on" resistance R_{don} (Ω)	0.087	
	Diode forward voltage drop U_{dth} (V)	1	
	Total referenced switching energy E_{sw} (J)	0.013	
	Temperature coefficient ε_{Ron} (1/°C)	0.0042	
	Temperature coefficient ε_u (1/°C)	0.003	
	Temperature coefficient ε_s (1/°C)	0.005	
Electric Motor (EM) (iron losses, cogging torque)	Steinmetz constant of hysteresis loss k_{hy}	5.8×10^{-3}	Referenced from literature[18]
	Steinmetz constant of eddy current loss k_{ed}	9.3×10^{-6}	
	Steinmetz constant γ	2	
	Factor of the maximum cogging torque λ	0.01	
	Temperature coefficient ε_{Rw} (1/°C)	0.0039	
Mechanical Power Transmission (MPT) (compliance, friction loss)	Nut-screw stiffness k_s (N/m)	3×10^8	From suppliers' datasheets
	Nut-screw damping d_s (N·s/m)	1×10^4	
	Coulomb friction force F_{cl} (N)	7590	Scaled from former experiments[42]
	Stribeck friction force F_s (N)	4702	
	Reference Stribeck speed v_{st} (m/s)	0.035	
	Mean coefficient of external force a	0.218	
	Quadrant coefficient b	0.13	

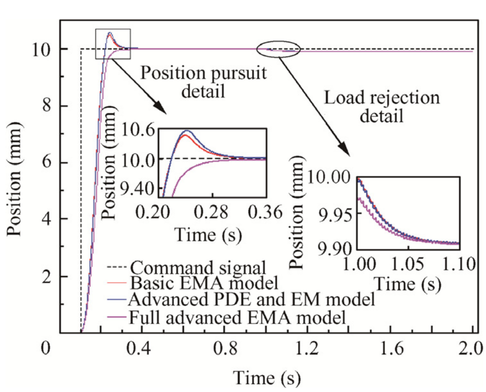

Fig. 13 Surface position response simulation.

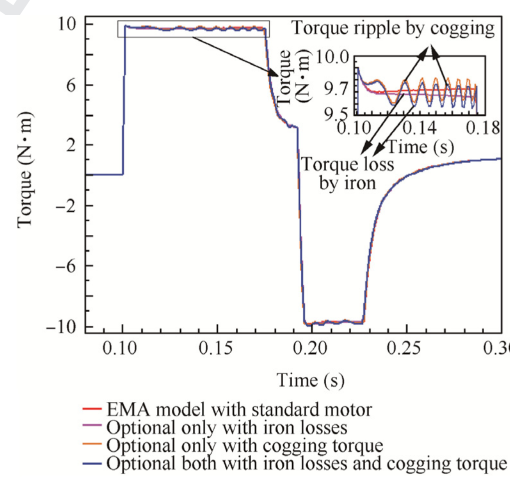

Fig. 14 Motor shaft torque simulation.

load is applied. Structural compliances at the anchorage of the EMA housing to the wing and at the EMA rod to load connection are merged into a single spring-damper model that is inserted in series between the rod and the load. The controller model implements the common structure of EMA controllers that was introduced in Section 2.2. Two saturation functions are generally inserted to limit the speed and the torque demands, possibly versus flight conditions. $\boldsymbol{G}_p(\boldsymbol{s})$ and $\boldsymbol{G}_v(\boldsymbol{s})$ are the position controller and velocity controller, respectively. The current controller $\boldsymbol{G}_i(\boldsymbol{s})$ is integrated in the PDE model. The $\boldsymbol{s}$ is the Laplace variable. Position feedback is rod displacement X_t (m), and the surface/load displacement is X_s (m).

4.2. Basic model for control synthesis

The basic model has to be simple and linear enough to facilitate the first step of control synthesis. At this level, thermal effects, electrical supply and fast dynamics are not considered. The PDE and EM make a pure electromagnetic torque generator. The dynamics of the current loop is introduced as a well-damped second order transfer function between the torque setpoint and the electromagnetic torque. Inertia and friction are not detailed at EMA component levels but merged

Please cite this article in press as: Jian F et al. Modelling and simulation of flight control electromechanical actuators with special focus on model architecting, multidisciplinary effects and power flows, *Chin J Aeronaut* (2016), http://dx.doi.org/10.1016/j.cja.2016.07.006

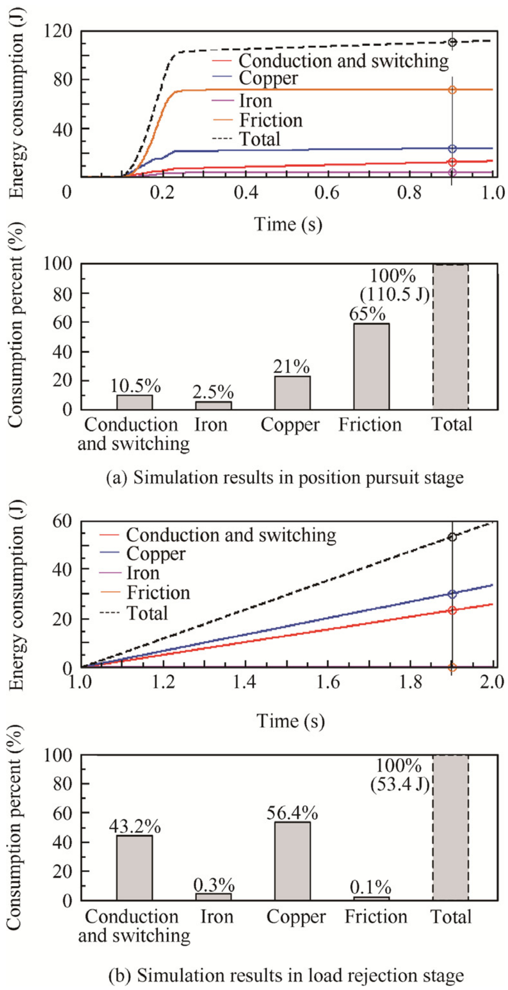

Fig. 15 Comparison of different energy losses.

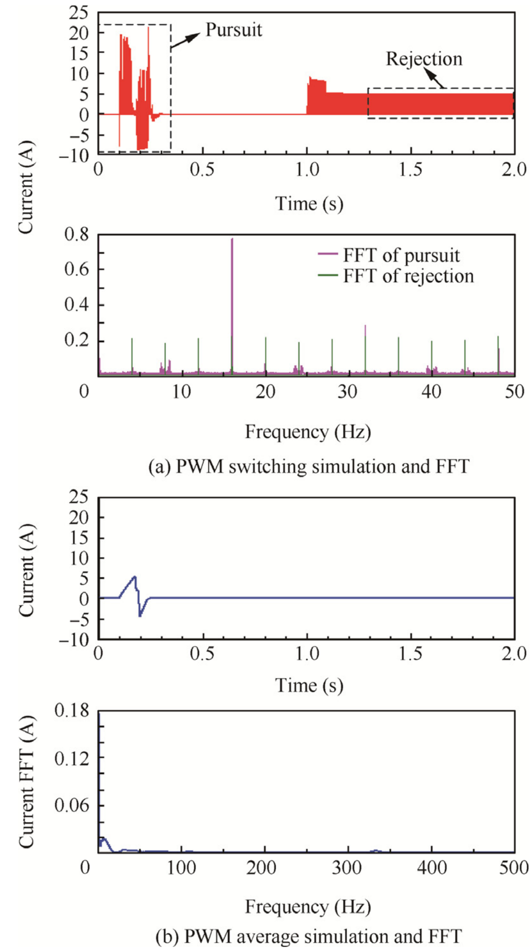

Fig. 16 Current pollution network comparison, PWM switching and PWM average.

into global effects. The EMA mechanical compliance is not introduced because it is not a major driver for control design. The resulting basic EMA model implemented in AMESim is presented in Fig. 10.

4.3. Realistic model with physical effects

The causal Bond-Graph of Fig. 8 is used to implement a realistic model considering multidisciplinary effects and power flows. According to the EMA physical architecture, the EMA model, Fig. 11, is split into three main sub-models: PDE, EM and MPT (Fig. 12). It clearly displays the interfaces for power (electric supply, mechanical anchorage and transmission to load, thermal environment), for signal (torque demand, output from sensors) and fault injection (jamming and free-run).

4.3.1. PDE simulation model

The PDE model architecture reproduces the structure of IGBT power management by the usual means of PWM on the DC supply input that provides a variable voltage to the three-arm inverter. The PWM signals are generated by a Clark/Park controller that links the 3-phase (A/B/C alternating current) reference frame to a rotating frame of two axes, direct and quadrature, in order to implement the field-oriented control[38] of the torque loop, as seen in Fig. 12(a). The I_{dref} and I_{q} are direct and quadrature axes of reference current (A) respectively. In order to make the simulation faster, an average model of the PWM can be used if there is no need to reproduce the dynamics associated with the switching frequency.[39] Conversely, at the expense of computer load, the model can be made even more realistic by introducing commutation delays and dead time, passive filters on the supply and motor lines, a supply rectifier and a chopper.

4.3.2. EM simulation model

The standard three-phase PMSM motor model is already integrated into the software model library. However, this model does not consider iron losses, cogging torque, magnetic saturation or hysteresis. Thus, a subcomponent is designed in Fig. 12 (b), which can replace the standard motor model. It implements Eqs. (13)–(16) using standard blocks from the library for signals (functions of one variable) and for mechanics (torque summation, friction, sensors). A specific model is created to provide a speed sum that corresponds to the 0 junctions in Fig. 8(b).

Please cite this article in press as: Jian F et al. Modelling and simulation of flight control electromechanical actuators with special focus on model architecting, multidisciplinary effects and power flows, *Chin J Aeronaut* (2016), http://dx.doi.org/10.1016/j.cja.2016.07.006

4.3.3. MPT simulation model

On the mechanical side, the perfect roller-screw is modelled using the generic nut-screw element. The friction loss is implemented with a generic piloted translational friction model that handles the numerical issues of breakaway properly. The level of friction force that pilots this element is formed as a function of the transmitted load, the sliding velocity and the temperature. It implements Eq. (19) in the simulation examples. A generic model that can be used to simulate preload or backlash as a function of a single parameter (x_0) is not available in the standard library. Such a model can be built according to Eq. (24) (elastic effect) and Eq. (25) (structural damping). The mechanical ports associated with anti-rotation of the screw and anti-translation of the nut are explicitly introduced for connection with the bearing and joint models. Jamming, wear or free-run faults are introduced as signals that can be used to modify the parameters of friction and compliance models. Fig. 12(c) shows the advanced model of MPT.

5. Model simulation for various engineering needs

In order to highlight the aspects of particular interest in the proposed model architecture and structure, an EMA driven aileron is simulated. The main parameters used in the following simulations are listed in Tables 2–4. The EMA model is run to illustrate how it can support six major engineering tasks: control design, energy consumption or thermal balance, pollution of power supply network, response to faults, failure of HUM and temperature sensitivity.

5.1. Control design

The closed-loop performance is usually assessed by quantifying stability, accuracy and dynamics for pursuit (output follows demand) and rejection (output is not affected by disturbances). For this purpose, an aileron position step demand of 10 mm (6% full stroke) is applied at time 0.1 s and then followed by a step aerodynamic force disturbance of 10 kN (40% rated output force) at time 1 s. Fig. 13 compares the simulated responses for three types of EMA models: (a) basic model, (b) advanced PDE and EM model except for MPT (applied by perfect transformer), and (c) full advanced model. Models (a) and (b) output globally the same response with only very little change in overshoot (1% of the step magnitude). Model (c) shows the importance of modelling friction accurately, for pursuit performance in particular. In addition,

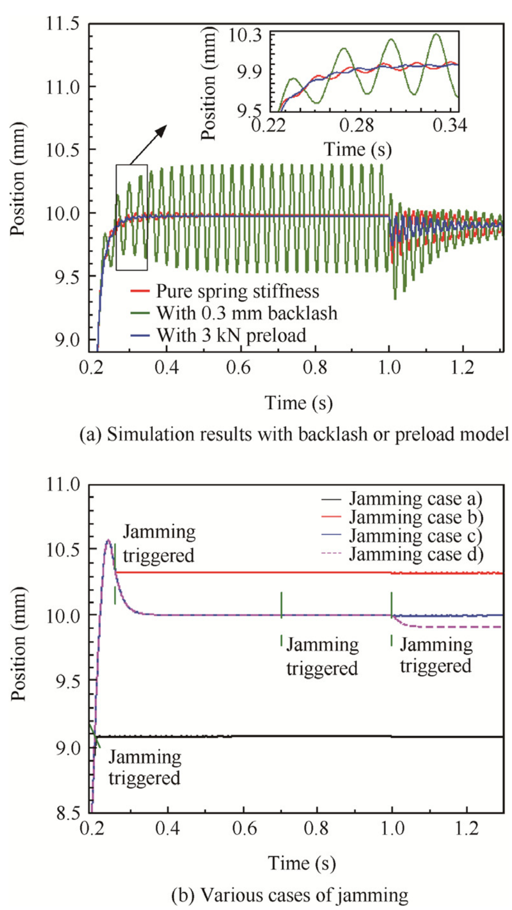

(a) Simulation results with backlash or preload model

(b) Various cases of jamming

Fig. 17 Surface position response when fault failure occurs for free-run and jamming.

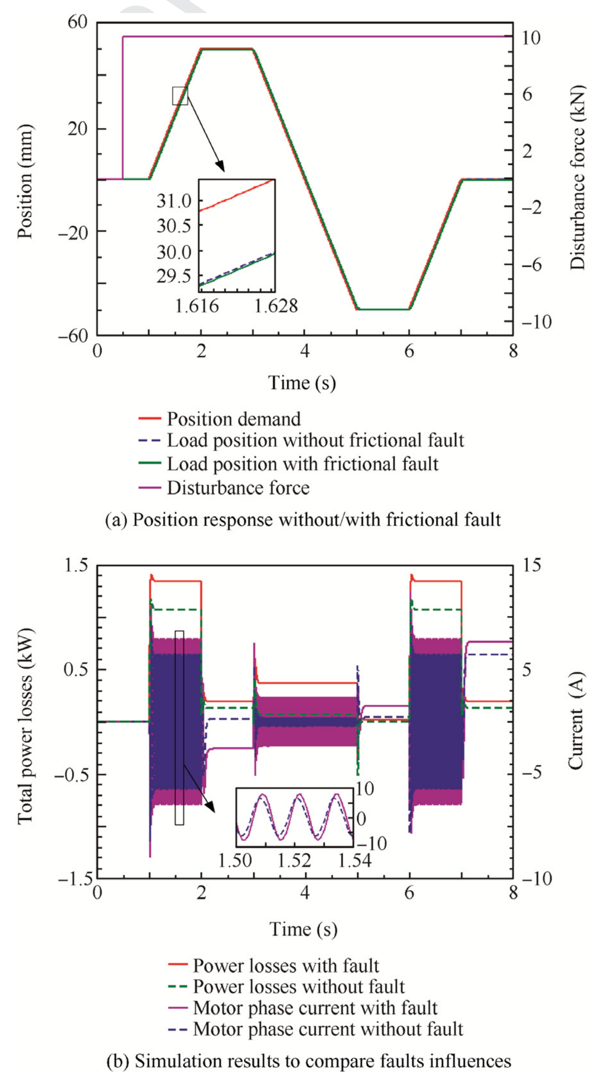

(a) Position response without/with frictional fault

(b) Simulation results to compare faults influences

Fig. 18 Surface position response when fault failure occurs for free-run and jamming.

it has to be borne in mind that, due to nonlinearity, responses change with pilot versus airload inputs. Fig. 14 displays the motor shaft torque simulated in four cases: (a) standard model without iron losses or cogging torque, (b) optional advanced model with iron losses only, (c) optional advanced model with cogging torque only, and (d) full advanced model with both iron losses and cogging torque. According to the magnitude of the position step demand, the current is saturated for 70 ms. The motor shaft torque is plotted versus time to highlight the differences, which are torque ripple and torque loss caused by cogging and iron effects, respectively.

5.2. Energy consumption analysis

The same model excitation is used for comparative analysis of energy loss and energy consumption (Fig. 15(a) for pursuit and Fig. 15(b) for rejection). In the absence of motion, when the final load position is reached, iron losses and friction losses become null. Copper and conduction losses remain present when the motor develops torque. Although friction represents the major source of energy loss, the importance of modelling conduction, switching and iron losses is highlighted: they represent up to 11% and 43.5% of total energy loss in the pursuit and rejection modes, respectively.

5.3. Power network pollution analysis

The effect of high frequency switching on driving the inverter arm with PWM is established by comparing the response of the full advanced model, Fig. 16(a) top, to that of a switching model, Fig. 16(b) top, where PWM is replaced by its low frequency equivalent. The PWM generates current spikes on the DC bus, the magnitude of which can reach several times the mean current. Spectrum analysis of the current through a fast Fourier transform (FFT) applied to the time history is displayed on the bottoms of the Fig. 16(a) and (b). For the switching model, it displays the first sub-harmonic and multiple harmonics of the PWM frequency (8 kHz). It should be remembered that the DC bus supply is considered perfect because it is out of the scope of the present work.

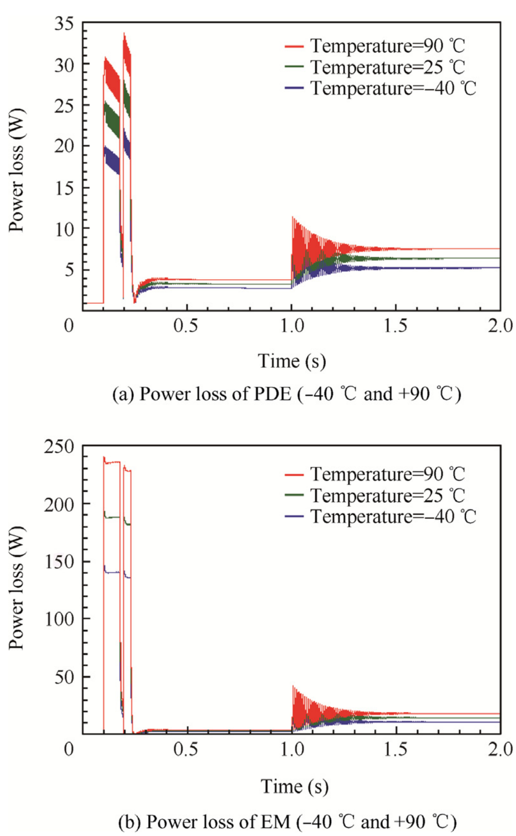

Fig. 19 Temperature sensitivity analysis for heat generation.

5.4. Analysis of wear/ageing and jamming faults

The analysis here focuses on the response to increased backlash and jamming faults. Fig. 17(a) compares the simulated responses of the advanced model for null preload or backlash (0.3 mm backlash), and a preload of 3 kN. Fig. 17(b) displays the simulated surface position when jamming is forced by adding a Coulomb friction (50 kN) at times: (a) 0.22 s (rise stage), (b) 0.27 s (overshoot stage), (c) 0.7 s (stability stage) and (d) 1.2 s (rejection stage). As expected, the position is frozen immediately.

5.5. Analysis of fault to failures for HUM

When focusing on analyses of fault failures to power losses or energy consumption in EMAs, a typical fault of MPT mechanism is selected, which reproduces augmentation of 50% friction force. In order to illustrate the influence of this fault, a specific mission is applied to the models, as shown in Fig. 18(a), using trapezoidal shapes for position demand (50 mm) and external load (10 kN). Firstly, the simulation result of Fig. 18(a) shows when introducing the fault in MPT, the position error becomes bigger (0.04 mm) than the no fault case. Secondly, as shown in Fig. 18(b), there are an additional 50% friction fault causes: more than 20% power losses and the maximum magnitude of the motor operating current increases nearly 23% for the opposite load (time 1–2 s and time 6–7 s). However, for adding load (time 3–5 s), the power losses increases to 5 times higher, and the motor operating phase current also becomes nearly 5 times larger; thus, the fault influence on an EMA is much more significant.

5.6. Temperature sensitivity analysis

In order to illustrate the ability of the proposed model architecture to simulate the effect of temperature, two figures are plotted below based on the model excitation as directed in Section 5.1. Fig. 19(a) displays the effect of temperature on PDE for heat generated by conduction losses and switching losses that increase by approximately 50% between −40 °C and + 90 °C. Fig. 19(b) shows the effect of temperature on EM for heat generated by copper loss that increases by 67% between the same operating temperature limits.

6. Conclusions

(1) The research presented in this paper is first aimed at architecting models for the system-level virtual prototyping of EMAs. Bond-Graphs were used to graphically

Please cite this article in press as: Jian F et al. Modelling and simulation of flight control electromechanical actuators with special focus on model architecting, multidisciplinary effects and power flows, *Chin J Aeronaut* (2016), http://dx.doi.org/10.1016/j.cja.2016.07.006

focus on the qualitative dependence between the multi-disciplinary and nonlinear effects that occur in power transmission from supply to driven load. The structure of the model calculation to be implemented in common simulation environments was developed by in-depth consideration of causality, which was facilitated by the introduction of causal marks in the Bond-Graphs.

(2) Since heat rejection is a key issue in the design of aerospace PbW actuators, system-level models were proposed for each source of energy loss in EMAs (power electronics, motor, mechanical transmission). Thermal ports were introduced into the models of components in order to explicitly expel the heat energy loss for each contributor. Additionally, the thermal port enabled models to be made sensitive to temperature and thus reproduce snow-ball effects.

(3) Due to the need to investigate response to failure, verify control robustness and assess HUM strategies, wear and fault models were proposed for mechanical power transmission devices. Jamming was simulated by forcing an increased level of Coulomb friction. Wear (or even free-run) was simulated by action on a single parameter that could be varied continuously to transit from preload to backlash.

(4) The proposed modelling approach was illustrated through the example of aileron actuation for a single-aisle commercial aircraft. The models were implemented in the AMESim simulation environment. It was shown that the above proposals provide engineers with models that can be developed in an incremental way with the advantage of keeping the same model structure during the various steps of simulation-aided development: conceptual design, control design, thermal balance and safety.

Acknowledgements

This study was supported by the Aeronautical Science Foundation of China (No. 2012ZD51) and the authors gratefully acknowledge the support of the China Scholarship Council (CSC).

References

1. Roboam X, Sareni B, Andrade AD. More electricity in the air: toward optimized electrical networks embedded in more-electrical aircraft. *IEEE Ind Electron Mag* 2012;**6**(4):6–17.
2. Rosero JA, Ortega JA, Aldabas E, Romeral L. Moving towards a more electric aircraft. *IEEE Trans Aerosp Electron Syst* 2007;**22**(3):3–9.
3. Botten SL, Whitley CR, King AD. Flight control actuation technology for next-generation all-electric aircraft. *Technol Rev* 2000;**8**(2):55–68.
4. Chakraborty I, Mavris DN, Emeneth M, Schneegans A. A methodology for vehicle and mission level comparison of More Electric Aircraft subsystem solutions: application to the flight control actuation system. *Proc Inst Mech Eng Part G – J Aerosp Eng* 2015;**229**(6):1088–102.
5. Yu X, Zhang Y. Design of passive fault-tolerant flight controller against actuator failures. *Chin J Aeronaut* 2015;**28**(1):180–90.
6. Todeschi M. Airbus-EMAs for flight controls actuation system-perspectives. In: *Proceedings of the international conference on recent advances in aerospace actuation systems and components*; 2010 May 5–7; Toulouse, France; 2010. p. 1–8.
7. Chakraborty I, Mavris DN. Integrated assessment of aircraft and novel subsystem architectures in early design*54th AIAA aerospace sciences meeting (SciTech); 2016 January 4–8*. San Diego, USA, Reston: AIAA; 2016.
8. Liscouët J, Maré J-C, Budinger M. An integrated methodology for the preliminary design of highly reliable electromechanical actuators: Search for architecture solutions. *Aerosp Sci Technol* 2012;**22**(1):9–18.
9. Takebayashi W, Hara Y. Thermal design tool for EHA. In: *Proceedings of the international conference on recent advances in aerospace actuation systems and components*; 2004 November 24–26; Toulouse, France; 2004. p. 15–20.
10. Faugère E, Maré J-C, Changenet C, Ville F, Delloue D. Coupling mechanical and thermal lumped parameters models for the preliminary design of power transmissions driven by thermal issues. In: *Proceedings of the 28th international congress on aerospace sciences*; 2012 September 23–28. Brisbane, Australia; 2012. p. 3690–700.
11. Dauphin-Tanguy G, Rahmani A, Sueur C. Bond graph aided design of controlled systems. *Simul Model Pract Theory* 1999;**7**(5–6):493–513.
12. Borutzky W. Bond graph modelling and simulation of multidisciplinary systems – an introduction. *Simul Model Pract Theory* 2009;**17**(1):3–21.
13. Dée G, Vanthuyne T, Alexandre P. An electrical thrust vector control system with dynamic force feedback. In: *Proceedings of the international conference on recent advances in aerospace actuation systems and components*; 2007 June 13–15. Toulouse, France; 2007. p. 75–9.
14. Fu J, Hazyuk I, Maré J-C. Preliminary design rules for electromechanical actuation systems – effects of saturation and compliances. In: *Proceedings of the 5th CEAS air & space conference*; 2015 September 7–11. Delft, Netherlands. Paper No.: CEAS-2015-057.
15. Rajapakse AD, Gole AM, Wilson PL. Electromagnetic transients simulation models for accurate representation of switching losses and thermal performance in power electronic systems. *IEEE Trans Power Deliv* 2005;**20**(1):319–27.
16. Feix G, Dieckerhoff S, Allmeling J, Schonberger J. Simple methods to calculate IGBT and diode conduction and switching losses. In: *Proceedings of the 13th European conference on power electronics and applications*; 2009 September 8–10. Barcelona, Spain.; 2009. p. 1–8.
17. Wang L, Maré J-C. A force equalization controller for active/active redundant actuation system involving servo-hydraulic and electro-mechanical technologies. *Proc Inst Mech Eng Part G – J Aerosp Eng* 2014;**228**(10):1768–87.
18. Krishnan R. *Permanent magnet synchronous and brushless DC motor drives*. 1st ed. USA: CRC Press; 2010. p. 92–122.
19. Attar B. *Modélisation réaliste en conditions extrêmes des servo-valves électrohydrauliques utilisées pour le guidage et la navigation aéronautique et spatiale[dissertation]*. INSA de Toulouse: Université de Toulouse; 2008.
20. Churn PM, Maxwell CJ, Schofield N, Howe D, Powell DJ. Electro-hydraulic actuation of primary flight control surfaces. In: *Proceedings of the IEEE colloquium on all electric aircraft*; 1998 June 17. London, UK; 1998. p. 3/1–3/5.
21. Krause PC, Wasynczuk O, Sudhoff SD, Pekarek S. *Analysis of electric machinery and drive systems*. 2nd ed. New York: John Wiley & Sons; 2013.
22. Monteiro JRBA, Oliveira AA, Aguiar ML, Sanagiotti ER. Electromagnetic torque ripple and copper losses reduction in permanent magnet synchronous machines. *Euro Trans Electr Power* 2012;**22**(5):627–44.
23. Exlar. Exlar product catalog, GSX series integrated motor/actuator; 2014. Available from: <http://exlar.com/pdf/?pdf=/content/uploads/2014/09/GSX-Catalog-Section1.pdf>.

Please cite this article in press as: Jian F et al. Modelling and simulation of flight control electromechanical actuators with special focus on model architecting, multidisciplinary effects and power flows, *Chin J Aeronaut* (2016), http://dx.doi.org/10.1016/j.cja.2016.07.006

24. Tellinen J. A simple scalar model for magnetic hysteresis. *IEEE Trans Magn* 1998;**34**(4):2200–6.
25. Casoria S, Sybille G, Brunelle P. Hysteresis modeling in the MATLAB/Power System Blockset. *Math Comput Simul* 2003;**63**(3–5):237–48.
26. Maré J-C. Best practices in system-level virtual prototyping: application to mechanical transmission in electromechanical actuators. In: *Proceedings of the 5th international workshop on aircraft system technologies*. 2015 February 24–25; Hamburg, German; 2015. p. 75–84.
27. Maré J-C. Friction modelling and simulation at system level: a practical view for the designer. *Proc Inst Mech Eng Part I – J Syst Control Eng* 2012;**226**(6):728–41.
28. Maré J-C. Friction modelling and simulation at system level: considerations to load and temperature effects. *Proc Inst Mech Eng Part I – J Syst Control Eng* 2015;**229**(1):27–48.
29. Jianyong Y, Wenxiang D, Zongxia J. Adaptive control of hydraulic actuators with LuGre model-based friction compensation. *IEEE Trans Ind Electron* 2015;**62**(10):6469–77.
30. Karam W, Maré J-C. Modelling and simulation of mechanical transmission in roller-screw electromechanical actuators. *Aircr Eng Aerosp Technol* 2009;**81**(4):288–98.
31. Balaban E, Bansal P, Stoelting P, Saxena A, Goebel KF, Curran S. A diagnostic approach for electro-mechanical actuators in aerospace systems. In: *Proceedings of the IEEE aerospace conference*; 2009 March 7–14. Big Sky, USA; 2009. p. 1–13.
32. Guo H, Xu J, Kuang X. A novel fault tolerant permanent magnet synchronous motor with improved optimal torque control for aerospace application. *Chin J Aeronaut* 2015;**28**(2):535–44.
33. Maggiore P, Dalla Vedova MD, Pace L, Desando A. Definition of parametric methods for fault analysis applied to an electromechanical servomechanism affected by multiple failures. In: *Proceedings of the second european conference of the prognostics and health management society*; 2014 July 8–10. Nante, France; 2014. p. 561–71.
34. Balaban E, Saxena A, Narasimhan S, Roychoudhury, Koopmans C, Ott C, et al. Prognostic health-management system development for electromechanical actuators. *J Aerosp Inf Syst* 2015;**12**(3):329–44.
35. Kagimoto H, Miyagi D, Takahashi N, Uchida N, Kawanaka K. Effect of temperature dependence of magnetic properties on heating characteristics of induction heater. *IEEE Trans Magn* 2010;**46**(8):3018–21.
36. Borutzky W. *Bond graph methodology: development and analysis of multidisciplinary dynamic system models*. London: Springer; 2010. p. 92–118.
37. Wang L. *Force equalization for active/active redundant actuation system involving servo-hydraulic and electro-mechanical technologies[dissertation]*. INSA de Toulouse: Université de Toulouse; 2012.
38. Krishnan R. *Electric motor drives: modeling, analysis, and control.* 1st ed. New Jersey: Prentice Hall Inc; 2001. p. 525–35.
39. Fu J, Maré J-C, Fu Y, Han X. Incremental modelling and simulation of power drive electronics and motor for flight control electromechanical actuators application. In: *Proceedings of the IEEE international conference on mechatronics and automation*; 2015 August 2–5. Beijing, China; 2015. p. 1319–25.
40. Clemente S. *Application characterization of IGBTs: international rectifier application note-AN-990*. International Rectifier Inc, 2012, Available from: <http://www.infineon.com/dgdl/an-990.pdf?fileId=5546d462533600a40153559fae19124e>.
41. ON Semiconductor, IGBT datasheet NGTB15N60EG. 2015, Available from: <http://www.onsemi.com/pub_link/Collateral/NGTB15N60E-D.PDF>.
42. Karam W. *Générateurs de forces statiques et dynamiques à haute puissance en technologie électromécanique[dissertation]*. INSA de Toulouse: Université de Toulouse; 2007.

Fu Jian is a Ph.D. candidate at the School of Mechanical Engineering and Automation, Beihang University, China. In September 2012, he was financed by the China Scholarship Council (CSC) to pursue his Ph.D studies in France. Currently, he is studying in the Institut Clément Ader (CNRS UMR 5312), INSA-Toulouse, France. His research interests are modelling, simulation and control of PbW actuation systems for aerospace applications.

Jean-Charles Mare is a professor and Ph.D. supervisor at the Institut Clément Ader (CNRS UMR 5312), INSA-Toulouse, France. He received his first degree in mechanical engineering in 1982 and his French Doctorat d'Etat in 1993. His current research activity deals with electrical actuation for flight controls, landing gears and engines. He has been involved in 4 European projects and 5 French competitiveness cluster projects dealing with electrical actuation in aerospace. He works closely with the aerospace industry, including Airbus, Goodrich, Latécoère, Messier and Turboméca, either for research programs or for scientific support. Since 1995, he has contributed to the design of various actuators test-benches (Eurocopter NH90, Airbus A340-600, A380 and A350, French strategic missile). He is now the chair of the International Conferences on Recent Advances in Aerospace Actuation Systems and Components (R3ASC). Since 1998, he has initiated and organized seven R3ASC conferences.

Fu Yongling is a professor and Ph.D. supervisor at the School of Mechanical Engineering and Automation, Beihang University, China. He received his Ph.D from Harbin Institute of Industry Technology in 1993. His areas of research include aircraft hydraulic transmission control design, industrial robots and efficient high-performance integrated electrohydraulic system manufacturing.

Please cite this article in press as: Jian F et al. Modelling and simulation of flight control electromechanical actuators with special focus on model architecting, multidisciplinary effects and power flows, *Chin J Aeronaut* (2016), http://dx.doi.org/10.1016/j.cja.2016.07.006